PNAS RESEARCH ARTICLE | MEDICAL SCIENCES

Evaluation of targeted and immune combination therapies in a rat model of hormone receptor–positive breast cancer

Ernesto Rojas-Jimenez[a,b,c], Triet M. Bui[a,b,c], Pengze Yan[a,b,c], Zheqi Li[a,b,c], Marco Seehawer[a,b,c], Jun Nishida[a,b,c], Pierre Foidart[a,b,c], Gordon J. Freeman[a,c], and Kornelia Polyak[a,b,c,1]

Contributed by Kornelia Polyak; received January 14, 2025; accepted December 30, 2025; reviewed by Jos Jonkers and Saraswati V. Sukumar

Estrogen receptor (ER) positive breast cancer is the most prevalent subtype, commonly responsive to endocrine therapies. Immune checkpoint inhibitors (ICIs) have limited efficacy in ER-positive disease, highlighting the need for the development of combination immunotherapies for these patients. We previously established that nitroso-N-methylurea-induced mammary tumors in outbred Sprague-Dawley rats mimic immune evasive mechanisms and the heterogeneity of ICI response observed in patients. We identified a "luminal growing" gene signature in ER-positive tumors, which correlated with tumor growth and immune-related differences. Here, we evaluated targeting candidates from this signature KMT5B/C and IKBKE using inhibitors A-196 and IKBKEi respectively, alongside anti-estrogen (fulvestrant) and a TGFβ blocking antibody (NIS793), both individually and in combination with αPD-L1, within this rat model. Fulvestrant emerged as the most effective treatment, inducing regression of most existing tumors and reducing on-treatment tumor burden when combined with αPD-L1. A-196, while ineffective as a monotherapy, demonstrated enhanced response when combined with αPD-L1. Comprehensive tumor profiling through polychromatic flow cytometry and single-cell RNA sequencing revealed that A-196 induced a luminal-to-basal shift in tumor epithelial cells, enhancing antigen presentation, whereas epithelial-to-mesenchymal transition was linked to fulvestrant resistance. Our findings underscore the value of the rat mammary tumor model for preclinical studies in ER-positive breast cancer and advocate for the further validation and potential clinical development of KMT5B/C inhibitors to enhance the efficacy and broaden the applicability of ICI therapy in cancer patients.

breast cancer | hormone receptor positive | immune checkpoint inhibitor | targeted therapy | endocrine therapy

Significance

The preclinical validation of novel therapies, particularly immunotherapies, in estrogen receptor (ER)-positive breast cancer has been constrained by the absence of suitable animal models that accurately replicate the human disease. Here we report the identification of the A-196 KMT5B/C inhibitor as a candidate potentiator of αPD-L1 efficacy in ER-positive NMU-induced rat mammary tumors, highlighting the usefulness of this preclinical model for the discovery and validation of novel therapies in breast cancer, especially in ER-positive disease.

Breast cancer is the most prevalent malignancy in women worldwide. Tumors are classified into subtypes based on the expression of estrogen (ER) and progesterone (PR) receptors and HER2, which guide treatment decisions. ER-positive tumors constitute the majority (~70%) of cases, particularly in postmenopausal women, and are treated with endocrine therapies alone or in combination with CDK4/6 inhibitors and other targeted therapies in more advanced cases (1, 2). Despite advancements in therapeutic strategies, challenges remain, as a subset of patients experience recurrence or do not respond to treatment. For patients unresponsive to standard of care, immunotherapy has shown promise. However, ER-positive breast cancers typically exhibited limited tumor-infiltrating lymphocytes and an abundance of immune-suppressive cells, reducing their likelihood of responding to immune checkpoint inhibitors (ICI) (3). The limited success of ICI in ER-positive disease underscores the importance of understanding and modulating cancer cell phenotypes and the tumor microenvironment (TME) to enhance therapeutic outcomes.

The development and testing of immunotherapies in ER-positive breast cancer have been hindered by the lack of immunocompetent animal models that accurately recapitulate the human disease. Carcinogen-induced rat mammary tumor models, developed and characterized over 50 y ago, are ER-positive and estrogen-dependent (4), but have been overlooked until recently due to challenges associated with their use, including the high number of mutations thought to be induced by the carcinogens and variability among animals in outbred strains. However, our recent comprehensive characterization of N-Nitroso-N-methylurea (NMU) induced mammary tumors in Sprague Dawley (SD) outbred rats demonstrated that the genetic mutation and gene expression profiles, and immune escape mechanisms of these tumors show remarkably high similarities to human breast cancer (5). Importantly, NMU-induced mammary tumors effectively mirror the molecular heterogeneity of human breast cancer with both ER-positive luminal and ER-negative basal tumors detected that display subtype-specific differences in response to combined TGFBR inhibitor and anti-PD-L1 (αPD-L1) treatment (5). Our studies

Author affiliations: [a]Department of Medical Oncology, Dana-Farber Cancer Institute, Boston, MA 02215; [b]Department of Medicine, Brigham and Women's Hospital, Boston, MA 02115; and [c]Department of Medicine, Harvard Medical School, Boston, MA 02115

Author contributions: E.R.J. and K.P. designed research; E.R.J., T.M.B., P.Y., M.S., J.N., and P.F. performed research; G.J.F. contributed new reagents/analytic tools; E.R.J., T.M.B., and Z.L. analyzed data; and E.R.J. and K.P. wrote the paper.

Reviewers: J.J., Antoni van Leeuwenhoek Nederlands Kanker Instituut; and S.V.S., Johns Hopkins University School of Medicine.

Competing interest statement: K.P. serves on the Scientific Advisory Board of Ideaya Biosciences, is an advisor to Curie. Bio and Novartis, holds equity in Antares Therapeutics and stock options in Ideaya Biosciences, receives sponsored research funding from Novartis, received honoraria from Astra-Zeneca and payment due to the acquisition of the mutant PIK3CA selective inhibitor program of Scorpion Biosciences by Eli Lilly. T.M.B. is a shareholder of Merck & Co., Novo Nordisk A/S, Eli Lilly & Co., AbbVie Inc., and Johnson & Johnson. G.J.F. has patents/royalties on the PD-L1/PD-1 pathway from Roche, Merck MSD, AstraZeneca, Bristol-Myers-Squibb, Merck KGA, Boehringer-Ingelheim, Dako, Leica, Mayo Clinic, Eli Lilly, and Novartis, has served on advisory boards for iTeos, NextPoint, IgM, GV20, IOME, Bioentre, Santa Ana Bio, Simcere of America, and Geode, and has equity in Nextpoint, iTeos, IgM, Invaria, GV20, Bioentre, and Geode.

[1]To whom correspondence may be addressed. Email: Kornelia_polyak@dfci.harvard.edu.

This article contains supporting information online at https://www.pnas.org/lookup/suppl/doi:10.1073/pnas.2501052123/-/DCSupplemental.

Published February 5, 2026.

further demonstrated that rats serve as valuable models for cancer prevention and aging studies, underscored by the human relevance of our findings (6, 7). Consequently, rat mammary tumor models are gaining renewed interest, particularly for studies of ER-positive cancer, due to the limited utility of current engineered mouse models, as most mouse mammary tumors are ER-negative, basal-like, and hormone-independent (4).

In a previous study using SD rats, we identified a "luminal growing signature" in ER-positive luminal mammary tumors that exhibited poor response to TGFBR inhibitor (LY2157299) and αPD-L1 treatment. This signature also correlated with immune-related differences and response to treatment in human ER-positive breast cancer (5). In this study, we explored whether targeting the genes and signaling pathways overactivated in these tumors could enhance the response to αPD-L1 treatment. Our objective is to generate preclinical data that could inform the development of novel therapeutic strategies, thereby expanding the applicability of ICIs in ER-positive breast cancer.

Results

Overview of the Model and Treatments. The luminal growing signature we previously described was enriched in ER-positive mammary tumors that grew in the αPD-L1 single agent or TGFBR inhibitor (Galunisertib/LY2157299) combination treatment arms, indicating a potential link to resistance against αPD-L1 (5). Thus, we hypothesized that combining inhibitors against genes in this signature with αPD-L1 might improve treatment responses. From the 38 genes comprising the signature, we selected candidates based on their established roles in cancer and immunotherapy responses, as well as the availability of suitable inhibitors for in vivo studies. We focused on IKBKE, a noncanonical I-kappa-B kinase recognized as an oncogene in breast cancer (8) and the KMT5C histone H4 lysine 20 trimethyl (H4K20me3) methyltransferase implicated in aging-related epithelial cell state changes (6), for further investigation. To inhibit IKBKE we used TBK1/IKKε-IN-5 (IKBKEi), which also targets TBK1 and was shown to improve response to αPD-L1 in mouse tumor models (9). For KMT5C we used the KMT5B/C-specific inhibitor A-196 (10). Additionally, we included fulvestrant, an ER antagonist, to verify the ER dependency of the tumors and to evaluate its immune effects both alone and in combination with αPD-L1. We also tested NIS793, a TGFβ blocking antibody (11), as an alternative to the previously used TGFBRI inhibitor (5), given that TGFβ blocking antibodies have been shown to improve response to anti-PD-1 treatment both in mice and humans (12). Tumors were induced by intraperitoneal NMU injection, resulting in palpable mammary tumor development in approximately 60 d (Fig. 1*A*, *SI Appendix*, Fig. S1*A*, and Dataset S1). Consistent with our prior study (5), all tumors were ER and PR positive by immunofluorescence and some had extensive stroma with high levels of extracellular matrix (ECM) proteins known to be induced by TGFβ such as decorin (*SI Appendix*, Fig. S1*B*).

Each compound was tested both as a single agent and in combination with αPD-L1 to investigate their ability to improve ICI response. Rats were randomized to one of the 10 treatment groups when a palpable tumor was detected and treatment duration was 4 and 6 wk for small molecule inhibitors (SMIs), and αPD-L1, respectively (Fig. 1*B*, *SI Appendix*, Fig. S1*A*, and Dataset S1), a treatment schema designed based on our prior results with TGFBR inhibitor (LY2157299) and αPD-L1 in this model (5). Throughout the experiment, we monitored the body weight of all animals from the start of treatment to the end of the study to assess potential drug-related toxicity (*SI Appendix*, Fig. S1*C*). Rats reaching Institutional Animal Care and Use Committee (IACUC) protocol endpoint criteria (e.g., weight loss, tumor size) were euthanized, under IACUC-approved protocol #15-055 and institutional SOP T017, resulting in earlier than planned treatment termination (i.e., incomplete treatment) for some animals (*SI Appendix*, Fig. S1*A*). In addition, due to the nature of this NMU-induced model, some animals developed additional tumors in different mammary glands after treatment was initiated. Therefore, we classified tumors into pretreatment and on-treatment groups (*SI Appendix*, Fig. S1*A*). Notably, while most treatment groups showed a consistent emergence of new tumors during the treatment period, the combination of fulvestrant and αPD-L1 resulted in a reduction in overall tumor burden (Fig. 1*C*) with fewer on-treatment tumors detected compared to vehicle (Fig. 1*D*), highlighting its potential to both suppress existing tumors and prevent new palpable tumor development.

Tumor onset was highly variable across rats making direct comparison of tumor volume between treatment groups challenging. Thus, we calculated tumor growth rate (5), a standardized measure of each individual tumor's growth as well as cumulative growth rates across treatment groups (Fig. 1*E* and *SI Appendix*, Fig. S1 *D* and *E*). Because some rats developed multiple tumors at different times, some tumors were exposed to treatment for only 1 wk, limiting the reliability of growth measurement. To ensure the accuracy of our assessment of tumor growth dynamics, we only included tumors with at least 2 wk of measurements. We found that only fulvestrant reduced cumulative growth rate significantly compared to the vehicle group (Fig. 1*E*). Next, we classified tumors as either stable or growing based on the median of the slope of the growth rate values (*SI Appendix*, Fig. S1*E*). Tumors across treatments, including even the control vehicle group, showed variability for stable and growing phenotypes, although the emergence of multiple tumors/animal and differences in length of tumor growth confounded this classification scheme. Accordingly, tumors with limited follow-up (≤1 wk), for which growth classification may not be reliable were not included in our quantifications and are denoted in the figure (Fig. 1*F*). Fulvestrant was the most effective monotherapy as most tumors in the fulvestrant-only treatment arm were stable or regressing (Fig. 1*F*). Responses to αPD-L1, NIS793, and IKBKEi single agent treatment were heterogenous with about half of the tumors classified as stable (Fig. 1*F*). The A-196 KMT5B/C inhibitor was the least effective as single agent with most (8/13) tumors classified as growing, but it showed an improvement in response with αPD-L1 combination, resulting in 8/13 tumors with stable phenotype (Fig. 1*F*).

To evaluate potential differences in tumor epithelial-stromal cell composition, we performed Masson's trichrome staining and quantified collagen and epithelial areas in each treatment group (*SI Appendix*, Fig. S1*F*). The fulvestrant group exhibited a significant reduction in epithelial content compared to vehicle likely due to its direct targeting of ER-positive cancer cells (Fig. 1*G*). In contrast, IKBKEi and αPD-L1 combination showed a decrease in collagen and a significant increase in epithelial content when compared to both vehicle and IKBKEi monotherapy (Fig. 1*G* and *SI Appendix*, Fig. S1*G*). Next, we analyzed tumor immune cell composition by polychromatic flow cytometry for myeloid and lymphocytic cell markers (*SI Appendix*, Figs. S2 and S3 and Table S1). The only significant difference we observed was an increase of $CD8^+$ T cells in the NIS793 and IKBKEi+αPD-L1 combination treatment group when compared to vehicle (Fig. 1*H* and *SI Appendix*, Fig. S4*A*), potentially due to the high variability among tumors within each treatment group.

To investigate treatment effects in further depth, we performed single-cell RNA-seq (scRNA-seq) on four tumors per treatment group selecting two growing and two stable tumors in each (*SI Appendix*, Fig. S1*D*), and six growing tumors from the vehicle,

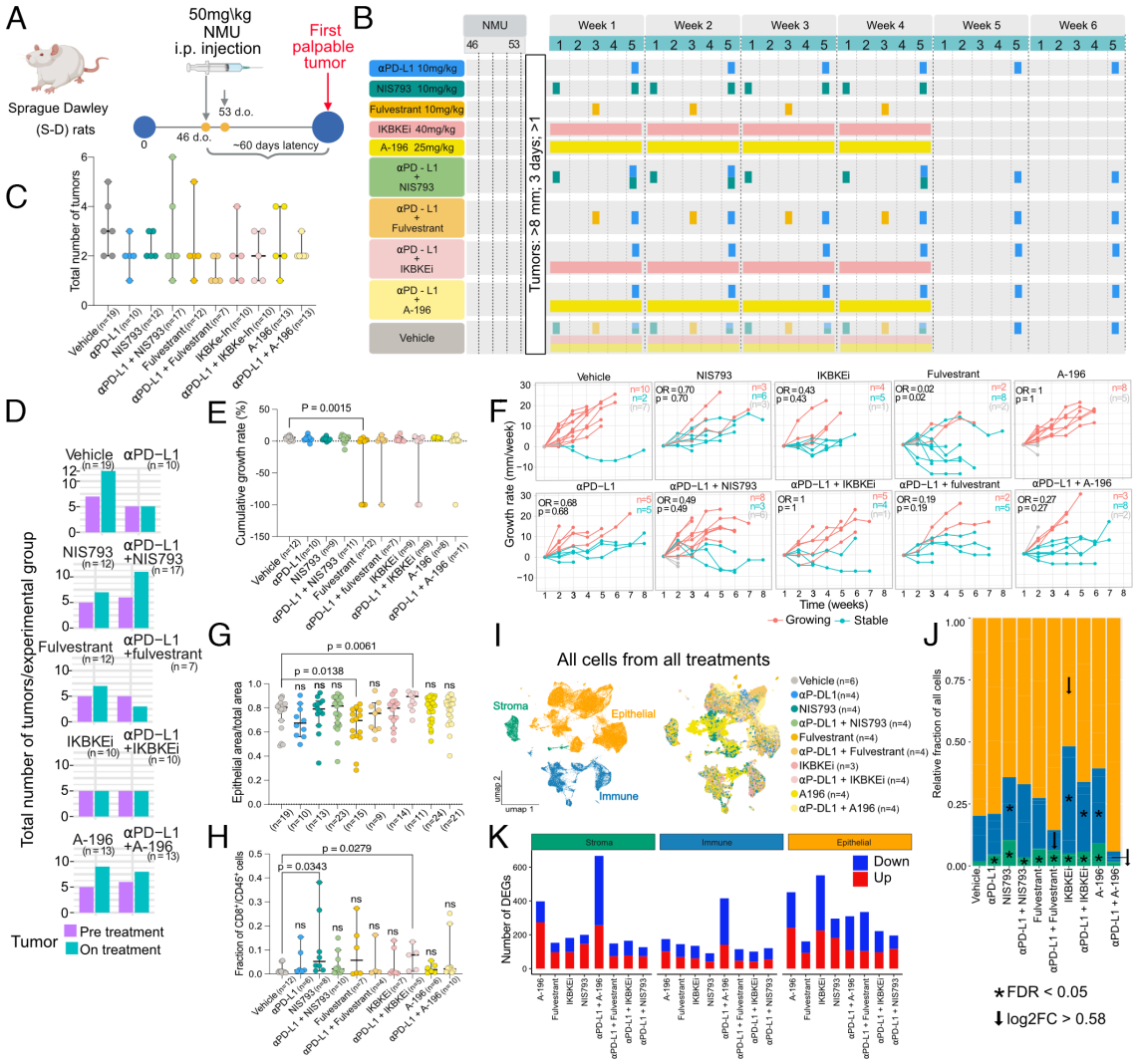

Fig. 1. Experimental design, tumor growth, and histology. (*A*) Schematic overview of experimental design. (*B*) Treatment groups and dosing schedules. Schematic representation of each treatment group, including drug names and doses, the timing of NMU administration, tumor eligibility criteria for treatment initiation, and weekly dosing schedule. (*C*) Jitter plots showing the total number of tumors by rat. Total number of tumors (n) in each group is indicated. (*D*) Bar plot showing the total number of pre- and on-treatment palpable tumors detected in each treatment group. (*E*) Cumulative growth rates across treatment groups, with median and 95% CI. P-values were calculated by Mann–Whitney *U* comparing each group by the vehicle. (*F*) Line plots represent individual tumors. Tumors with sufficient size measurements (≥2 wk) were classified as growing (red) or stable (blue) based on linear regression of tumor volume over time, while tumors with ≤1 wk of monitored growth are depicted in gray. Odds ratios indicate the likelihood of a tumor being classified as "growing" vs. "stable" in each treatment group relative to the vehicle group. *P*-values and OR were calculated using Fisher's exact test relative to the vehicle group. (*G*) Jitter plots depicting quantification of epithelial areas, with median and 95% CI. Quantifications include measurements from tumor sections, with multiple sections taken from large tumors to capture intratumoral heterogeneity. *P*-values were calculated by Mann–Whitney *U* comparing each group by the Vehicle. (*H*) Graph showing the relative proportions of $CD8^+$ $CD45^+$ viable cells quantified by flow cytometry, with median and 95% CI. *P*-values were calculated by the Kruskal–Wallis test. (*I*) UMAP visualization of scRNA-seq data from all treatment groups. Cells are colored by major compartments: epithelial, stromal, and immune (*Left*), and by treatment group (*Right*). (*J*) Stacked bar plots showing the relative proportions of epithelial, stromal, and immune cell populations in each treatment group. (*K*) Bar plots showing the number of significantly differentially expressed genes (DEGs) (adjust *P* value <0.05, |Log2FC| > 0.5) in each treatment group compared to vehicle based on. Note: Differences in cell population frequencies in scRNA-seq data were assessed using a permutation test (1,000 permutations) in all figures. Log2 fold change CI were estimated via bootstrapping. Populations with FDR < 0.05 and |log-2FC| > 0.58 were considered significant. Significant increase and decrease compared to the vehicle is marked with an asterisk (*) and a down arrow (↓), respectively.

four of which were from a pilot study, merged and integrated with our current dataset. Across all treatments, we identified 20 distincT cell clusters that we categorized into tumor epithelial, stromal, and immune subsets based on lineage and subtype-specific markers (Fig. 1*I*, *SI Appendix*, Fig. S4 *B* and *C* and Table S2, and Dataset S2). The relative fraction of tumor epithelial cells was lower in most single agent treatment compared to vehicle, while the combination groups of fulvestrant and A-196 with αPD-L1 showed a pronounced decrease in immune cell fraction compared to both vehicle and single agent groups (Fig. 1*J*), suggesting immune-scarce phenotypes. Differential expression analysis revealed treatment-induced changes in transcriptional profiles in each of the three major cellular fractions (i.e., epithelial, stroma, and immune), where A-196 alone or in αPD-L1 combination showed the most pronounced changes in stroma and immune compartments and IKBKEi in the epithelial subset (Fig. 1*K*). Next, we analyzed each treatment module (i.e., vehicle, αPD-L1, SMI, and combination) individually to deconvolute treatment-specific changes in cellular and molecular profiles.

The Effects of NIS793 and IKBKEi. Unsupervised clustering of the NIS793 treatment module revealed 13 distinct clusters based on the expression of cell type–specific markers (*SI Appendix*, Fig. S5*A* and Dataset S3). Quantification of the relative fraction of these populations showed a significant increase in $CD4^+$ and $CD8^+$ T cells, and luminal progenitor-like (LP-like) tumor epithelial cells, a reduction in basal tumor epithelial cells and antigen-presenting (e.g., dendritic cells) cell populations across all treatments (*SI Appendix*, Fig. S5*B*). Assessment of TGFβ signaling pathway activity by gene set enrichment analysis showed higher levels in stromal and immune cells compared to tumor epithelium, but no significant differences due to treatment in any compartment (*SI Appendix*, Fig. S5 *C* and *D*). Subclustering of the stromal compartment did not show any NIS793-related differences in cellular composition (*SI Appendix*, Fig. S5 *E* and *F*, and Dataset S3), whereas in the tumor epithelium there was a significant decrease in basal tumor cells in the NIS793-treated group (*SI Appendix*, Fig. S5 *G* and *H*, and Dataset S3), consistent with the known

growth promoting role of TGFβ in this cell type (13). Among the immune cell populations, the NIS793-treated group showed the most pronounced differences in T cells, especially $CD4^+$ T cells, where we detected significantly fewer Tregs and an increase in a $CD4^+$ T cell cluster (CD4 IFN) enriched for interferon-related genes compared to other groups (*SI Appendix*, Fig. S5 *I–M*, and Dataset S3). Chronic type I interferon responses have been associated with $CD8^+$ T cell dysfunction (14). Consistent with this, the expression of exhaustion markers (*Pdcd1*, *Lag3*, *Havcr2*, and *Tigit*), was higher in the CD8 effector ($CD8^+$ Eff) cluster in the NIS793 treatment group (*SI Appendix*, Fig. S5*N*).

IKBKEi treatment had the most pronounced effects on the tumor epithelial and immune cells, particularly $CD4^+$ T cells and luminal progenitor-like (LP-like) tumor epithelial cells, impacting both cellular composition and transcriptional profiles (Fig. 1 *J* and *K*, *SI Appendix*, Fig. S6 *A* and *B*, and Dataset S4). Gene set enrichment analysis revealed that multiple inflammatory and immune-related hallmark signature scores were higher in IKBKEi-treated tumors, particularly in macrophages, stroma, $CD4^+$ T cells, and tumor epithelial cells (*SI Appendix*, Fig. S6*C*). Analysis of the TNF-α signaling via NF-κB signature, a pathway targeted by IKBKEi, revealed markedly higher activity in tumors treated with IKBKEi, both as a single agent and in combination with αPD-L1 likely driven by the increase in luminal progenitor-like (LP-like) tumor epithelial cells showing the highest enrichment (*SI Appendix*, Fig. S6 *D* and *E*). More detailed analyses of the tumor epithelial subclusters confirmed significantly higher fraction of LP-like tumor cells in the IKBKEi and luminal cells in the combination treatment groups (*SI Appendix*, Fig. S6 *F–H*, and Dataset S4). Pathway analysis highlighted immune inflammatory, E2F target, TNF-α signaling via NF-κB, IL6/JAK/STAT3, IFN, and complement pathway scores as enriched in LP-like and IM clusters in the IKBKEi monotherapy group (*SI Appendix*, Fig. S6 *I* and *J*). Increase in the expression of *Irf1*, a master transcription factor in the TNF-α via NF-κB pathway induced by IFN-γ, was particularly prominent in luminal and LP-like tumor epithelial cells (*SI Appendix*, Fig. S6*K*).

Among immune cells we observed higher relative proportion of $CD4^+$ T cells along with fewer tumor-associated macrophages (TAM) in the IKBKEi monotherapy group (*SI Appendix*, Fig. S6 *L* and *M*, and Dataset S4). Subclustering of the myeloid population, where most of the immune pathway changes were observed, revealed that the relative proportion of tissue-resident TAM cluster was significantly higher in the IKBKEi monotherapy group, while alternative activated TAM (aaTAM) was more prominent in the αPD-L1 treatment arm (*SI Appendix*, Fig. S6 *N* and *O*, and Dataset S4). TNF-α signaling via NF-κB hallmark scores were also elevated in myeloid cells in the IKBKEi monotherapy (*SI Appendix*, Fig. S6*P*). Flow cytometry quantification demonstrated a significant increase in M2 $RT1B^+$ (MHCII) macrophages in the combination treatment group compared to vehicle (*SI Appendix*, Fig. S6*Q*).

Overall, tumors in both NIS793 and IKBKEi treatment groups exhibited differences in tumor cellular composition and transcriptomic profiles when compared to vehicle controls, but none of these alterations showed significant association with tumor growth phenotypes.

Mechanisms of Fulvestrant Response and Resistance. Fulvestrant was the most effective single agent treatment resulting in tumor regression in most cases (Fig. 1 *E* and *F*), confirming the dependency of the tumors on estrogen and ER. Analysis of the fulvestrant module scRNA-seq data revealed the most pronounced differences in tumor epithelial cells and T cells (*SI Appendix*, Fig. S7 *A* and *B*). We observed five distinct tumor epithelial cell clusters with varying composition across treatments (Fig. 2 *A* and *B* and *SI Appendix*, Fig. S7*C*, and Dataset S5 and S6). The fraction of LP-like tumor cells was significantly higher in each treatment group compared to vehicle with the most pronounced difference observed with fulvestrant monotherapy, while luminal cancer cells predominated in the combination treatment subset (Fig. 2*B*). We performed MiloR neighborhood analysis (15) to assess differences in tumor epithelial cell populations in relation to tumor growth dynamics and found significant overlap and structural differences between growing and stable tumors (Fig. 2 *C* and *D*). We then assigned these neighborhoods to the cell clusters previously annotated in the UMAP and found that neighborhood composition varied markedly across treatment groups, reflecting treatment-dependent changes of the epithelial compartment (*SI Appendix*, Fig. S7 *D* and *E*). Hallmark pathway analysis demonstrated that neighborhoods enriched in growing tumors showed activation of hormone receptor–related pathways (late estrogen response, E2F targets) and cancer-associated programs such as epithelial-to-mesenchymal transition (EMT), suggestive of a transcriptional shift toward basal-like epithelial cell states. In contrast, neighborhoods enriched in stable tumors were related to inflammatory and metabolic signatures, including TNF-α signaling via NF-κB and oxidative phosphorylation (Fig. 2*E*). Consistent with these transcriptional changes, immunofluorescence staining for luminal (KRT18) and basal (KRT14, SMA) markers demonstrated a significant reduction of both KRT14 and KRT18 in the fulvestrant group, whereas in the combination arm only the KRT18+ cells were significantly decreased (Fig. 2 *F* and *G*). Further investigation of differences in luminal-basal cell states revealed an increase of basal gene signature in LP-like cells in the combination therapy and in the luminal cluster in the fulvestrant treatment groups (*SI Appendix*, Fig. S7*F*). Subclustering of luminal tumor epithelial cells uncovered additional cell populations including an androgen receptor positive (AR+) subset enriched in the combination treatment and intermediary cells more frequent in the fulvestrant-only arm (Fig. 2 *H* and *I*, and Dataset S6). To investigate AR-positive tumor cells in further detail, we performed immunofluorescence for AR and ER, and CD3 T cell marker. We observed significantly more AR+ epithelial cells within tumors in both fulvestrant single agent and combination groups (Fig. 2 *J* and *K*). To assess whether AR expression in tumor cells is associated with endocrine therapy response in the clinic, we analyzed RNA sequencing data from a cohort of ER positive breast cancer patients subject to prolonged neoadjuvant aromatase inhibitor treatment (16). Patients were classified as responders or nonresponders based on a Preoperative Endocrine Prognostic Index (PEPI) score ≥ 4 and/or disease recurrence after a median follow-up of 58 mo. We found that AR expression was significantly higher in tumors from patients classified as responders compared to nonresponders (Fig. 2*L*). These results are in line with prior studies reporting that AR expression in early-stage breast cancer is associated with favorable clinical outcomes (17).

Next, we analyzed putative mechanisms of fulvestrant resistance by identifying differences between growing and stable tumors in the vehicle and fulvestrant treatment groups. Specifically, we selected genes that were overexpressed in growing compared to stable tumors within the vehicle or within the fulvestrant group and designated genes uniquely overexpressed in the fulvestrant group as a fulvestrant-resistance signature (Fig. 2*M*). The signature included several genes with known roles in endocrine resistance, including *Esr1*, *Pgr*, and *Nfkb1* (20–22). Tumor epithelial cell clusters more abundant in growing tumors had higher expression of this "fulvestrant-resistance signature" supporting the role of these genes in therapeutic resistance (*SI Appendix*, Fig. S7*G*).

To validate the clinical relevance of our fulvestrant-resistance signature, we analyzed its expression in ER-positive breast tumors in a Phase II neoadjuvant clinical trial of anastrozole, fulvestrant, and gefitinib (18). A marked shift in the signature distribution was observed between pretreatment and posttreatment samples in both responsive and nonresponsive cases, with nonresponsive samples exhibiting consistently higher scores (Fig. 2*N*). We

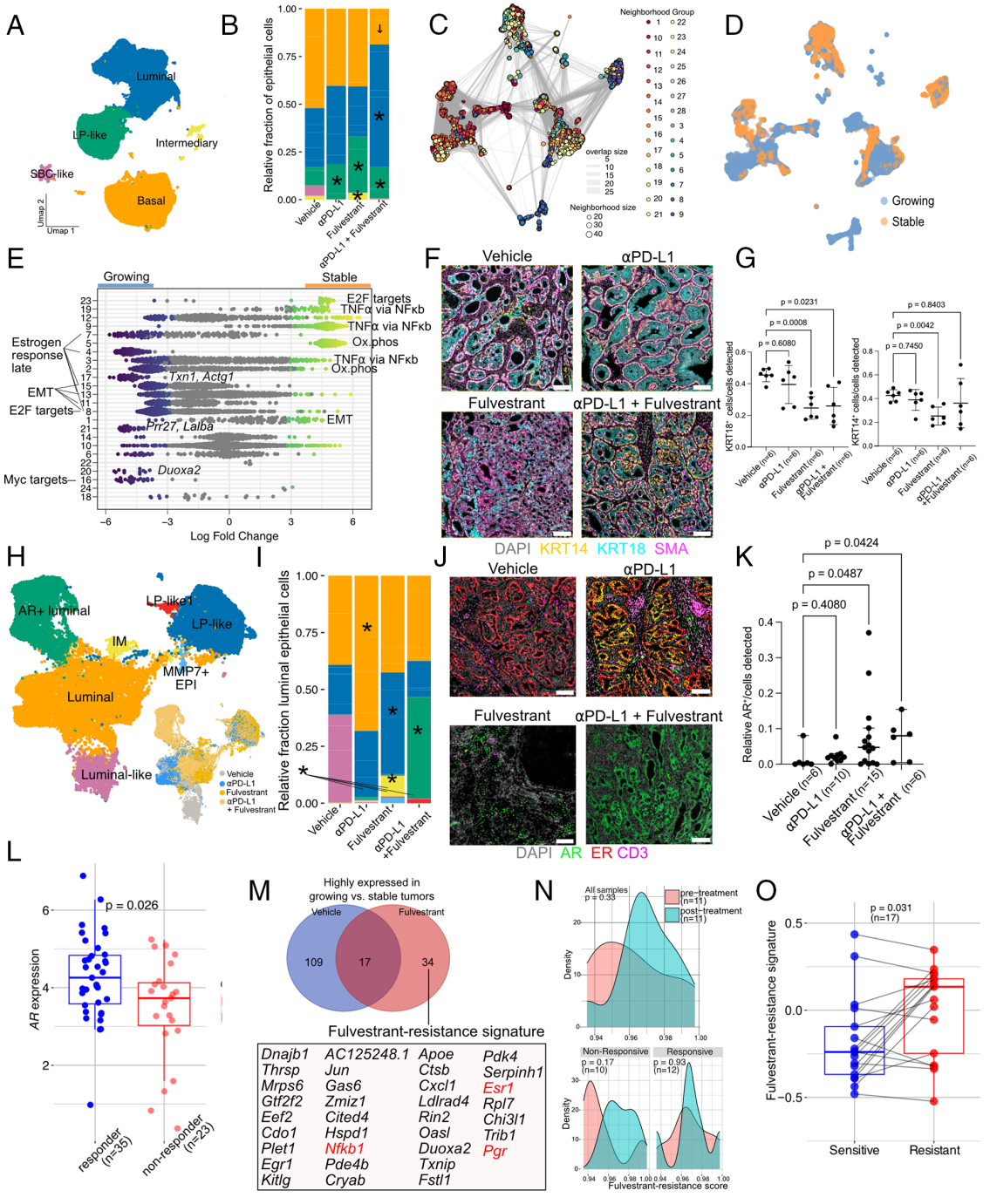

Fig. 2. Molecular and cellular characterization of Fulvestrant-treated tumors. (*A*) UMAP visualization of tumor epithelial cell clusters. (*B*) Stacked bar plots depicting relative proportions of cancer cell clusters in each treatment group. (*C*) MiloR neighborhood analysis of tumor epithelial cells. Circle size proportional to neighborhood size, connecting lines indicate overlap between neighborhood with thickness reflecting overlap magnitude. (*D*) MiloR UMAP with neighborhoods colored for growing and stable tumor classification. (*E*) Beeswarm plot of differential abundance between growing and stable tumors across MiloR neighborhoods. Each point represents a neighborhood-specific sample, with the *x*-axis showing the log fold change in cell abundance between growing and stable tumors. Groups are annotated with representative marker genes and enriched Cancer Hallmark pathways. (*F*) Representative images of immunofluorescence for KRT14, KRT18, and SMA in tumors from each treatment group. DAPI used to stain nuclei. Scale bar is 104 μm. (*G*) Jitter plot showing the percentage of KRT18+ or KRT14+ cells relative to the total number of detected cells per sample. Each point represents one sample (n = 6 per treatment group). Median and 95% CI are indicated. *P*-values were calculated using the Brown–Forsythe and Welch ANOVA test. (*H*) UMAP of luminal tumor epithelial cell subclustering colored by clusters (*Left*) or treatment (*Right*). IM-intermediary. (*I*) Stacked bar plots showing the relative proportions of luminal subclusters in each treatment group. Colors correspond to clusters in the UMAP. (*J*) Representative images of immunofluorescence for AR, ER, and CD3 in tumors from each treatment group. DAPI used to stain nuclei. Scale bar is 100 μm. (*K*) Jitter plot depicting the quantification of AR+ cells as a percentage of total detected cells. Each point represents one sample. Median and 95% CI are indicated. *P*-values were calculated by the Kruskal–Wallis test. (*L*) Boxplot showing AR expression in responder and nonresponder groups from the Guerrero-Zotano et al. clinical cohort (16) *P*-value was calculated with the Wilcoxon test. (*M*) Venn diagram showing overlap of genes highly expressed in luminal-like cells in growing tumors within vehicle and fulvestrant treatment groups. This latter set of genes we defined as "fulvestrant-resistance signature." (*N*) Density plots showing the distribution of endocrine resistance signature expression across all samples, and nonresponding and responding patients. Each plot includes separate curves for pre- and posttreatment signatures defined by Massarweh et al. (18) *P* value was calculated with the *U* Mann Whitney test. (*O*) Paired point plots comparing endocrine resistance signature scores between sensitive and resistant cases from Xia et al. (19) *P*-value was calculated with the Wilcoxon test. Note: Differences in cell populations frequencies in scRNA-seq data were assessed using a permutation test (1,000 permutations) in all figures. Log2 fold change CI were estimated via bootstrapping. Populations with FDR < 0.05 and |log2FC| > 0.58 were considered significant. Significant increase and decrease compared to the vehicle is marked with an asterisk (*) and a down arrow (↓), respectively.

further investigated another recently published neoadjuvant ER-positive breast cancer cohort with sequential collection of on-treatment biopsies identified as either responsive or resistant toward endocrine treatment (19). We found significantly higher fulvestrant-resistance signature enrichment levels in resistant tumors compared to the intrapatient paired responsive tumors (Fig. 2*O*).

Last, we analyzed the immune cell populations and observed a predominance of $CD4^+$ $Foxp3^+$ regulatory T cells (*SI Appendix*, Fig. S7 *H–L*, and Dataset S5). All treatment groups showed a slight increase in memory $CD8^+$ T cells compared to vehicle, while the combination therapy group specifically exhibited an increase in memory $CD4^+$ and activated $CD4^+$ T cells (*SI Appendix*, Fig. S7*L*). In the myeloid cell fraction, we observed a decrease in

anti-inflammatory macrophages (anti-Inf Mac) in treatment groups including fulvestrant, while both groups with αPD-L1 demonstrated an increase in DCs (*SI Appendix*, Fig. S7 *M–O*, and Dataset S5). These results suggest that the fulvestrant and αPD-L1 combination therapy not only enhances T cell activation but also reprograms the myeloid compartment, potentially favoring a more effective antitumor immune response.

The Impact of Fulvestrant and Anti–PD-L1 on the Normal Mammary Gland. The fulvestrant + αPD-L1 combination was not only effective to inhibit the growth of existing tumors but was also the only treatment that reduced the emergence of new on-treatment palpable tumors implicating a potential cancer preventive effect (Fig. 1*D*). Thus, we investigated the impact of this combination as well as each single agent on the normal mammary glands of rats exposed to NMU, but without palpable tumors. Histological analysis revealed frequent small hyperplastic lesions in the fulvestrant and vehicle groups, two out of five and one out of six mammary glands, respectively, while mammary glands from αPD-L1 and combination-treated rats had very few epithelial cells, and none had hyperplastic lesions (Fig. 3 *A* and *B* and *SI Appendix*, Fig. S8*A*).

To investigate the cellular and molecular basis underlying these histological differences, we performed scRNA-seq on representative mammary glands from the fulvestrant and combination treatment groups (*SI Appendix*, Fig. S8*A*), while we used scRNA-seq data of vehicle controls from our prior study (7). UMAP showed a significant reduction in the epithelial cell proportion in the combination group compared to both vehicle and fulvestrant monotherapy (Fig. 3 *C* and *D*, and Dataset S7). GSEA using hallmark gene sets on all cells/treatment group showed strong enrichment for proliferative pathways such as MYC and E2F targets, G2M checkpoint, and PI3K/AKT/MTOR signaling in the vehicle samples, with concomitant reduction in both fulvestrant and combination groups, whereas apoptosis-related pathways were enriched in the combination-treated glands (*SI Appendix*, Fig. S8*B*). Module scoring confirmed that proliferative pathways were most active in epithelial cells of vehicle control, while the combination group displayed the highest apoptosis scores in epithelial cells, potentially explaining the reduced epithelial cell content in this group (Fig. 3*E*).

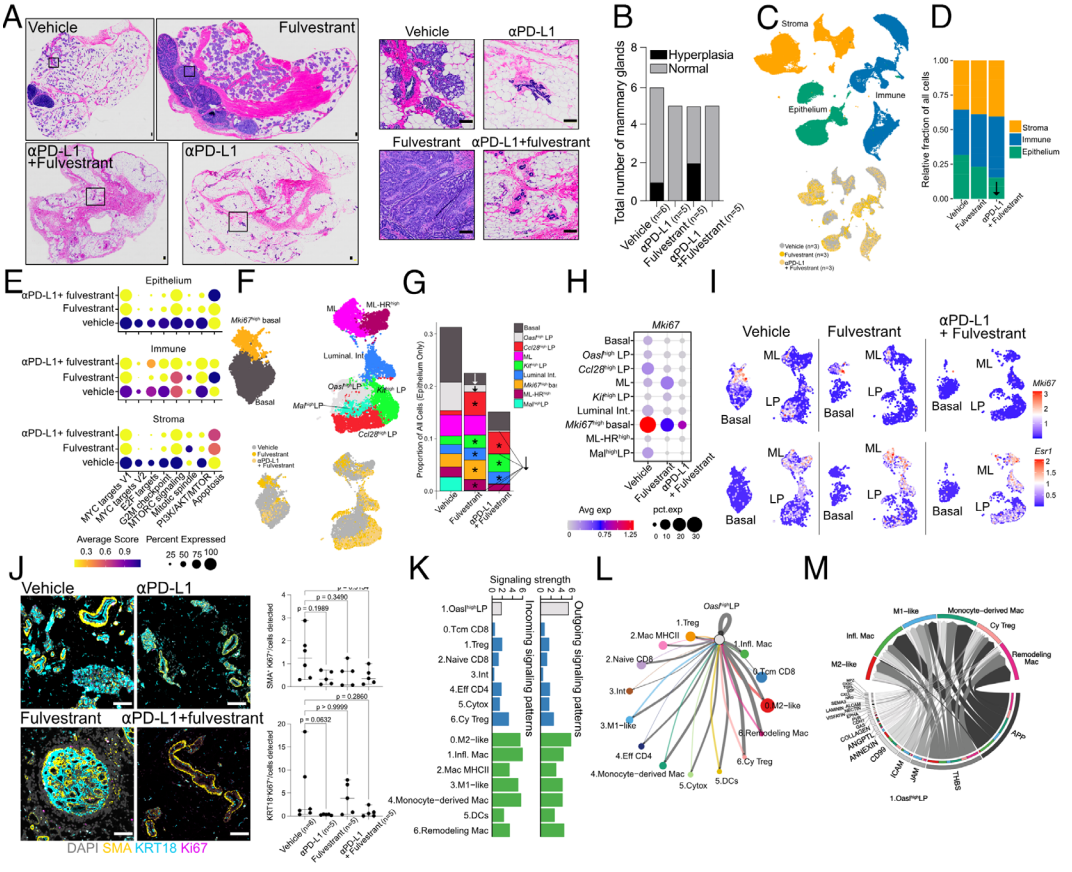

Fig. 3. Cellular and molecular insights from the normal mammary gland in the Fulvestrant treatment module. (*A*, *Left*) Representative whole-section hematoxylin-eosin-stained images of mammary glands from each treatment group. (*Right*) High-magnification insets corresponding to the black-boxed areas in the left panel. Small hyperplastic lesions are visible in the fulvestrant-treated glands. (Scale bar, 100 μm.) (*B*) Bar plot summarizing the number of animals with histologically normal glands or hyperplasia across treatment groups. (*C*) UMAP visualization of all mammary gland cells showing the main cellular compartments: epithelium, stroma, and immune. Accompanying UMAP colored by treatment highlights sample distribution across the three groups. (*D*) Stacked bar plot showing the relative proportions of the main compartments across treatments. The arrow indicates significant decrease in epithelial cell abundance. (*E*) Dot plot showing the enrichment scores and expression levels of selected Hallmark pathways across treatments, split by major cell compartment. (*F*) UMAP of epithelial cells colored for annotated subclusters (*Top*) or treatment (*Bottom*). (*G*) Stacked bar plots showing the relative abundance of epithelial cells across treatment conditions. Bars represent the total proportion of all cells per condition, with each segment indicating the proportion of individual epithelial cell subclusters within the epithelial compartment. (*H*) Dot plot showing the percentage of *Mki67* and their average expression, stratified by treatment and epithelial cell clusters. (*I*) UMAP feature plots of *Mki67* (*Top*) and *Esr1* (*Bottom*) expression across tumor epithelial cells. Plots are split by treatment, with major clusters labeled to illustrate treatment-specific expression patterns. (*J*) Representative immunofluorescence images of SMA, KRT18, and Ki67 staining of tumors from each treatment group (*Left*). (Scale bar, 100 μm.) Quantification of Ki67-positive cells in KRT18+ (luminal) and SMA+ (stromal) populations, shown as jitter plots with median and 95% CI (*Right*). Each point represents one sample. *P*-values were calculated using the Kruskal–Wallis test. (*K*) Bar plot showing the total incoming and outgoing signaling strength of each cluster, as inferred by CellChat. Bars are colored by major cell type (white, epithelial cluster (*Oasl*^{high} LP); blue, T cells; and green, Myeloid cells), with cluster names indicated on the *y*-axis. (*L*) Network plot depicting the predicted cell–cell communication network with *Oasl*^{high} LP as the sender. Nodes represenT cell populations, with node size proportional to their overall communication strength. Directed edges represent ligand–receptor interactions, with edge width corresponding to interaction strength. (*M*) Chord diagram illustrating the predicted outgoing interactions from the Oasl^{high} LP epithelial cluster toward the top recipient populations (M2-like, Infl. Mac, M1-like, Monocyte-derived Mac, Cy Treg, and Remodeling Mac). Each ribbon represents a signaling pathway, with ribbon width proportional to the relative contribution of that pathway to the total outgoing communication. Within each pathway ribbon, colored subdivisions indicate the proportion of signaling directed to each receiver. Note: Differences in cell populations frequencies in scRNA-seq data were assessed using a permutation test (1,000 permutations) in all figures. Log2 fold change CI were estimated via bootstrapping. Populations with FDR < 0.05 and |log2FC| > 0.58 were considered significant. Significant increase and decrease compared to the vehicle is marked with an asterisk (*) and a down arrow (↓), respectively.

Epithelial subclustering revealed several clusters nearly absent in the combination group, including *Mki67*^{high} basal, ML, and *Oasl*^{high} LP cells, while several LP subclusters, like *Ccl28*^{high} LP and *Kit*^{high} LP, were expanded in fulvestrant-treated glands (Fig. 3*F*, and Dataset S7). Although overall epithelial abundance increased in the fulvestrant group, ML and basal cells were reduced, while a *Mki67*^{high} and *Cdkn2a*^{high} basal cluster with progenitor features was specifically enriched (Fig. 3 *G* and *H*). UMAP feature plots further showed higher *Esr1* expression within the residual ML population, most prominently in the fulvestrant-treated group, suggesting treatment-resistant residual ML cells (Fig. 3*I*). These transcriptional findings were corroborated by immunofluorescence, which showed a trend toward fewer Ki67^{+}SMA^{+} cells in fulvestrant-treated glands (Fig. 3*J*).

Oasl^{high} LP cells displayed differential enrichment for genes involved in immune-related processes. To better understand their impact on other cellular compartments, we performed cell–cell communication analysis using CellChat (23, 24) (*SI Appendix*, Fig. S8*D*). First, we examined interactions between this epithelial cluster and the two major nonepithelial fractions, immune and stromal cells, to identify the dominant communication routes. Oasl^{high} LP cells exhibited strong outgoing signaling toward the stromal compartment, particularly through extracellular matrix pathways such as laminin and collagen. Thrombospondin (THBS) signaling emerged as a major outgoing pathway from Oasl^{high} LP cells to both stromal and immune compartments. Amyloid precursor protein (APP) signaling was uniquely directed toward the immune compartment, consistent with a known role of this pathway in inflammation (25).

Given the prominent stromal and immune signaling observed from Oasl^{high} LP cells, we next examined the composition of all these cellular compartments, to contextualize these interactions. In the stromal compartment, we observed an increase in both inflammatory and matrix fibroblasts in the treatment arms, with a decrease in endothelial and pericyte fractions (*SI Appendix*, Fig. S8 *E* and *F*, and Dataset S8). Within immune cells, the frequency of both B and T cells was significantly lower in the fulvestrant monotherapy group compared to vehicle with the opposite observed with combination treatment (*SI Appendix*, Fig. S8 *G* and *H*, and Dataset S8). In contrast, macrophage populations, especially MHCII-high macrophages, were elevated in the fulvestrant group. More detailed analysis of T cells showed a statistically significant increase of effector CD4^{+} T cells in the fulvestrant group compared to vehicle (*SI Appendix*, Fig. S8 *I* and *J*, and Dataset S8), while myeloid cell subclustering revealed an increase in M2-like and monocyte-derived macrophages, and a decrease in inflammatory and remodeling macrophages in the combination group (*SI Appendix*, Fig. S8 *K* and *L*, and Dataset S8). Building on the prominent interactions between Oasl^{high} LP cells and the immune compartment, we next analyzed communication between this epithelial cluster and specific immune subpopulations. The analysis of signaling strength, which reflects the overall intensity of outgoing and incoming communication per cluster, revealed robust outgoing signaling from Oasl^{high} LP cells, with myeloid cells also showing substantial communication activity (Fig. 3*K*). When Oasl^{high} LP cells acted as the source, the strongest interactions were directed toward myeloid populations, followed by Tregs (Fig. 3*L*). We therefore examined the specific ligand–receptor pathways mediating these interactions. Among the top pathways were amyloid precursor protein (APP) and thrombospondin (THBS) signaling, as well as junctional adhesion molecule (JAM), intercellular adhesion molecule (ICAM), and CD99 pathways (Fig. 3*M*).

Together, these findings suggest that the combination of fulvestrant and αPD-L1 not only reduces epithelial cell proliferation and promotes apoptosis but also reshapes the immune microenvironment in a manner that eliminates tumor-prone epithelial cell states and dampens immunosuppressive epithelial–immune interactions. The coordinated loss of specific epithelial cell clusters with immunoregulatory features, coupled with reduced myeloid infiltration and restored T cell proportions, supports a model in which combination therapy prevents the progression of early-stage tumors by disrupting protumor epithelial and immune niches.

The Impact of KMT5B/C Inhibition on Cellular Phenotypes and Response to αPD-L1. Next, we investigated the molecular and cellular effects of the A-196 KMT5B/C histone H4K20 methyltransferase inhibitor (26, 27) on mammary tumors. Immunofluorescence staining for H4K20me3 showed high levels in tumor epithelial cells and a significant reduction in H4K20me3-positive cells after A-196 treatment confirming effective KMT5B/C inhibition (Fig. 4 *A* and *B*). This reduction was not observed in the combination treatment group (Fig. 4 *A* and *B*) likely because tumors were collected 2 wk after stopping A-196 treatment while continuing αPD-L1 administration (*SI Appendix*, Fig. S1*A*).

UMAP of scRNA-seq revealed several unique tumor epithelial cell subpopulations that we classified as progenitor-like A-196 (PL-A) and luminal progenitor-like A-196 (LPL-A) and were most abundant in the A-196 monotherapy group (Fig. 4 *C* and *D* and *SI Appendix*, Fig. S9*A*, and Dataset S9). GSEA on all cells revealed that the TNF-α signaling via NF-κB pathway showed the most significant increase in enrichment in the A-196 treatment group with the reverse observed in the combination treatment arm (*SI Appendix*, Fig. S9*B*). Several other immune and inflammation-related pathways including IL6/JAK/STAT3 and IFN-γ signaling were also highly expressed in the A-196 treatment group, together with apoptosis (*SI Appendix*, Fig. S9 *B* and *C*). TNF-α signaling via NF-κB signature scores were the highest in fibroblasts and macrophages, and in a subset of luminal tumor epithelial cells (Fig. 4*E*).

Due to the emergence of unique tumor epithelial subclusters in the A-196 single agent group, we investigated treatment-associated changes in epithelial cells in further detail. Subclustering identified eight major clusters, including basal, luminal, luminal progenitor-like (LPL), and alveolar-like (AL), and PL-A and LPL-A populations only seen in the A-196 group together with significant expansion of LPL and LPL-2 cells (Fig. 4*F* and *SI Appendix*, Fig. S9 *D* and *E*, and Dataset S10). All luminal populations showed an increase in the TNF-α signaling via NF-κB hallmark signature scores in the A-196 monotherapy group (*SI Appendix*, Fig. S9*F*). The appearance of more progenitor-like PL-A and LPL-A cells in A-196 treatment group suggested perturbations in epigenetic programs defining luminal cell states. In line with this, we observed a decrease in the Gini index score of several basal-specific genes including *Acta2* and *Krt14*, in LPL cells implying a shift to basal phenotype (higher expression in more cells) (Fig. 4*G*). This change in Gini index was not detected in other epithelial clusters analyzed (*SI Appendix*, Fig. S9*G*), indicating that A-196 treatment mainly affects LPL tumor cells. We also calculated cell-to-cell transcriptomic distances to assess cellular heterogeneity and found the highest baseline levels in LPL cells, which was decreased in the A-196 single agent and combination treatment groups, suggesting cell state homogeneity of treated LPL cluster (*SI Appendix*, Fig. S9*H*). Consistent with increased *Acta2* and *Krt14* expression, we observed increased basal signature scores in the LPL subcluster in A-196 single agent and combination treatment groups (Fig. 4*H*). To validate these predictions, we performed immunofluorescence for luminal (KRT18) and basal (KRT14) cytokeratins. We detected a decrease in KRT18-positive cells in both A-196 single agent and αPD-L1 combination groups (Fig. 4 *I* and *J*). Intriguingly, the luminal-to-basal shift was associated with increased expression of antigen presentation signature (Fig. 4*H*), which could explain the improved efficacy of the A-196 and αPD-L1 combination to suppress tumor growth compared to each single agent alone.

Analysis of immune cell populations revealed six major clusters, with myeloid and B cells being more prominent in the A-196 monotherapy group, while combination treatment showed a depletion of all immune cell clusters, suggesting immune scarcity or exclusion (Fig. 4 *K* and *L* and *SI Appendix*, Fig. S9*I*, and Dataset S9). TNF-α signaling via NF-κB hallmark signature scores were elevated across the myeloid cells, especially in macrophages, in the A-196 monotherapy group (Fig. 4*M*). Within the myeloid populations the fraction of M2-like macrophages was lower in the combination treatment arm with concomitant increase in monocytes, whereas mast cells showed elevated levels in the A-196 monotherapy group (Fig. 4 *N* and *O*, and Dataset S9). MHC II signature scores were significantly higher in myeloid subclusters in the combination therapy group, indicating enhanced antigen-presenting potential of the remaining myeloid cells (Fig. 4*P* and *SI Appendix*, Fig. S9*J*). Flow cytometry confirmed this finding with the combination therapy group exhibiting significantly higher proportion of tissue macrophages with high MHC II (RTB1) expression (*SI Appendix*, Fig. S9*K*). Exhaustion markers (e.g., *Tox*) in $CD8^+$ T cells and Treg markers (e.g., *Foxp3* and *Tnfrsf4*) in $CD4^+$ T cells were higher in the A-196 monotherapy group and lower with combination treatment (*SI Appendix*, Fig. S9 *L* and *M*).

In the A-196 and αPD-L1 combination-treated tumors, we observed an increased epithelial fraction accompanied by a marked decrease in immune cells by scRNA-seq, despite improved tumor control relative to A-196 alone. GSEA of epithelial cells revealed a reduction in inflammatory programs, including TNFα signaling

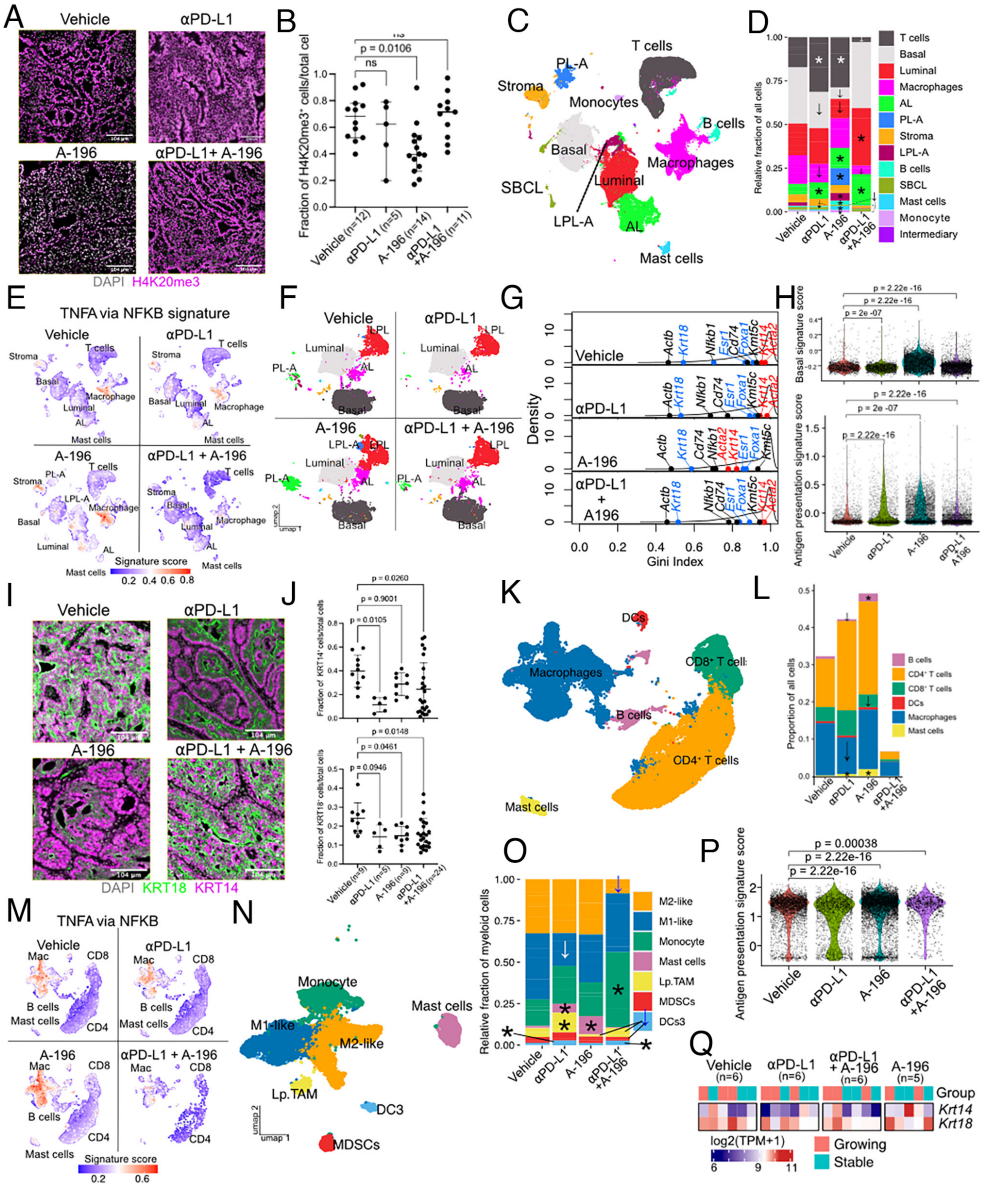

Fig. 4. Molecular and cellular effects of A-196 treatment. (*A*) Representative images of immunofluorescence staining for H4K20me3 in tumors from each treatment group. DAPI used to stain nuclei. Scale bar is 104 μm for all panels. (*B*) Graph depicting quantification of H4K20me3-positive cells, with median and 95% CI. *P*-values were calculated by the Kruskal–Wallis test. (*C*) UMAP of all cells from the A-196 treatment module. Alveolar-like (AL), Progenitor-like in A-196 (PL-A), Luminal Progenitor-like in A-196 (LPL-A), secretory basal cell-like (SBCL). (*D*) Stacked bar plots showing the relative proportions of the clusters. (*E*) Feature plots displaying enrichment scores for the TNF-α signaling via NF-κB Hallmark signature across all clusters. UMAPs are split by treatment group, with major clusters annotated to show treatment-specific differences in pathway activity. (*F*) UMAP of tumor epithelial cells across groups. Subclusters: Luminal, Basal, Luminal Progenitor-like (LPL), Alveolar like (AL), and Progenitor like in A196 (PL-A), and Luminal Progenitor-like (LPL-A) which were clusters mostly present only in the A-196 single treatment group (green and blue). (*G*) Density plot showing the Gini index for each gene within the LPL cluster in each treatment group. Selected luminal and basal cell type–specific genes are highlighted in blue and red, respectively. (*H*) Basal and antigen presentation signature scores within the LPL subcluster. *P*-values were calculated by Mann–Whitney *U* comparing each group to vehicle. (*I*) Representative images of immunofluorescence staining for KRT18 and KRT14 in tumors from each treatment group. DAPI is used to visualize nuclei. Scale bar is 104 μm. (*J*) Quantification of KRT18-positive cells as a percentage of total detected cells, with median and 95% CI. *P*-values were calculated by the Kruskal–Wallis test. (*K*) UMAP depicts immune cells. Subclusters: CD4 and CD8 T cells, macrophages (Mac), B cells, and masT cells. (*L*) Stacked bar plots showing the relative abundance of immune cells across treatment conditions. Bars represent the total proportion of immune cells per condition, with each segment indicating the proportion of individual immune cell subclusters within the immune compartment. (*M*) Feature plots displaying enrichment scores for the TNF-α signaling via NF-κB Hallmark signature across the immune cell populations in each treatment condition. (*N*) UMAP of myeloid cells. Subclusters: M2-like, M1-like, Monocytes, masT cells, tumor-associated macrophages with lipid metabolism (Lp TAM), myeloid derived suppressor cells (MDSCs), and dendritic cells type 3 (DC3). (*O*) Stacked bar plots showing the relative proportions of the indicated myeloid cell clusters in each treatment condition. (*P*) Violin plots showing the expression of antigen presentation signature score in each treatment group. (*Q*) Heatmap, split by sample, displaying $\log_2$(TPM + 1) expression levels of *Krt18* and *Krt14* across individual tumor samples. Grouped (Stable vs. Growing) is indicated in the top annotation. Note: Differences in cell populations frequencies in scRNA-seq data were assessed using a permutation test (1,000 permutations) in all figures. Log2 fold change CI were estimated via bootstrapping. Populations with FDR < 0.05 and |log2FC| > 0.58 were considered significant. Significant increase and decrease compared to the vehicle is marked with an asterisk (*) and a down arrow (↓), respectively.

via NF-κB and the Inflammatory Response hallmark (*SI Appendix*, Fig. S9*B*). To further explore the underlying intercellular dynamics, we analyzed the inferred cell–cell communication between the most prominent epithelial cluster enriched in the combination group and the immune subsets (*SI Appendix*, Fig. S9*N*). This analysis revealed strong interactions between epithelial and myeloid cells, which was confirmed by examining the overall interaction strength across clusters (*SI Appendix*, Fig. S9*O*). Notably, myeloid-directed interactions such as APP-CD74 and GAS were preserved (*SI Appendix*, Fig. S9*P*). CD99 and GAS interactions were also observed exclusively in the αPD-L1–treated tumors. Together, these data support a model in which A-196 and αPD-L1 combination therapy suppresses tumor-intrinsic NF-κB–driven chemokine production, thereby reducing lymphocyte infiltration while maintaining selective communication with myeloid cells.

To complement our scRNA-seq findings on a limited set of samples with more comprehensive profiling of additional tumors, we performed bulk RNA-seq on six tumors per treatment group. Differential expression analysis identified minimal statistically significant differences (*SI Appendix*, Fig. S9*Q*), likely due to the limited power of bulk RNA-seq to detect consistent differences among heterogeneous tumors. Among all comparisons, the greatest transcriptomic differences were observed between the vehicle and combination treatment groups, with upregulated genes including *Cst12*, *Nrgn*, and *Duoxa2*, and downregulation of genes related to antigen presentation such as *RT1-BB* (*SI Appendix*, Fig. S9*Q*). The second most distinct comparison was between vehicle and αPD-L1, again highlighting *Cst12* and *Nrgn* as upregulated targets, suggesting that αPD-L1 may be driving a substantial portion of the transcriptional response.

To evaluate epithelial differentiation states, we classified tumors as hormone receptor (HR) high or low using a curated set of luminal and basal markers (*Esr1, Krt18, Foxa1, Gata3, Krt14, Acta2*, and *Ar*). We also calculated the Krt14/Krt18 TPM ratio to further assess epithelial plasticity. Notably, four of five tumors in the A-196 group were classified as HR^{high} yet exhibited among the highest *Krt14/Krt18* ratios (*SI Appendix*, Fig. S9 *R* and *S*). Although not statistically significant, this trend suggests a basal-like shift despite high HR expression, consistent with the luminal-to-basal transition observed via Gini index analysis in our scRNA-seq dataset. When directly comparing log2(TPM+1) expression of *Krt14* and *Krt18* (Fig. 4*Q*), tumors from the A-196 group showed a coordinated increase in both genes, contrasting with other treatment groups where *Krt14* tended to decrease. Only three vehicle-treated samples exhibited a similar expression pattern to A-196. Together, these findings suggest that A-196 monotherapy may promote epithelial reprogramming toward a hybrid luminal-basal state and immunosuppressive features, effects that appear to be mitigated by combination treatment with αPD-L1.

Discussion

The introduction of immune checkpoint inhibitors has revolutionized the treatment of many cancer types leading to durable responses even in metastatic disease (28). In breast cancer the addition of pembrolizumab (αPD-1) to chemotherapy has significantly improved the outcomes of patients with PD-L1-positive triple-negative breast cancer (TNBC) (29). The effectiveness of ICI in ER-positive breast cancer, the most common subtype has been inadequate (30, 31), although more recent studies suggest that a subset of patients with ER-positive tumors may benefit from ICI combinations, highlighting the need for patient selection (32), and improving our understanding of the ER-positive breast tumor immune environment to design rational combination therapies. Progress in this area has been hindered by the lack of immunocompetent preclinical models that enable the development of these novel treatments. We previously described the exceptional utility of the ER-positive NMU-induced rat mammary tumor model for testing ICI therapies (5). Here, we used this model to test the combination of αPD -L1 with targeted agents selected based on our previous study implicating them in resistance to αPD -L1 and TGFBR inhibition (5). Specifically, we tested IKBKE and KMT5B/C inhibitors along with fulvestrant ER antagonist and NIS793 TGFβ blocking antibody and identified the A-196 KMT5B/C inhibitor as a candidate potentiator of ICI therapies in ER-positive breast cancer. Despite its advantages, the NMU-induced rat mammary tumor model also has several limitations. There is high variability among tumors potentially due to the use of an outbreed strain and differences in mutations likely influenced by normal cell-of-origin and immune editing. However, the resemblance of immune escape mechanisms and ICI responses to human breast cancer makes this model useful for the preclinical testing of novel immunotherapies in ER-positive breast tumors.

Contrary to our previous findings and those of others, which indicated an enhanced response to ICI with TGBR inhibition (5, 33), the NIS793 TGF-β-targeting monoclonal antibody did not significantly impact tumor growth or cellular phenotypes, either alone or in combination. This highlights the complexities of targeting TGFβ, although the limited efficacy of the anti-human TGF-β antibody against rat TGF-β cannot be ruled out. Notably, NIS793 treatment led to a reduction in basal tumor cells and regulatory T cells, consistent with the established role of TGFβ in regulating these cell types (34). Aligning with our findings, the initial Phase I/Ib clinical trial of NIS793, both alone and in combination with spartalizumab (αPD-1 antibody) in advanced solid tumors, demonstrated a favorable safety profile but limited clinical efficacy, despite achieving on-target effects (35). Similarly, we observed modest effects on tumor growth and phenotypes with either IKBKEi alone or in combination with αPD-L1, aside from a shift to a more proinflammatory state and activated NF-κB signaling as revealed by scRNA-seq. The IKBKEi we used also inhibits TBK1 (TANK-binding kinase 1), a gene identified as a driver of immune evasion and potentiator of αPD-L1 treatment efficacy, partly by enhancing sensitivity to TNF and IFNγ (9, 27). Given these opposing functions, exploiting IKBKE/TBK1 and NF-κB signaling for cancer treatment necessitates a more detailed mechanistic understanding of their effects in specific cell types.

Fulvestrant emerged as the most effective single-agent treatment, inducing regression of most tumors. As an ER degrader, fulvestrant exerted the most pronounced effects on tumor epithelial cells, promoting a shift toward more alveolar-like phenotypes and enhancing the expression of *Esr1*, *Pgr1*, and *Nf-kb* in tumors that were growing and presumably resistant to treatment. These findings align with genomic analyses of fulvestrant response and resistance in advanced ER-positive breast cancer, which indicates increased EGF pathway and FOXA1 signaling, as well as the expression of *TFAP2C*, a known transcriptional regulator of ER activity, as predictors of response (36), validating the clinical relevance of our rat model. Intriguingly, we detected an AR+ luminal cell type in residual tumors from rats treated with fulvestrant and αPD-L1 combination. Previous clinical studies have demonstrated that AR expression in early-stage luminal tumors is associated with improved outcomes (17, 37, 38), supporting the hypothesis that AR-positive cells may represent a favorable population in this context. Similarly in a patient cohort subject to prolonged neoadjuvant aromatase inhibitor treatment AR expression was elevated in the tumors of responders (16).

Although the combination of fulvestrant with αPD-L1 was not more effective than fulvestrant alone in inhibiting the growth of

existing tumors, it was the only treatment arm that reduced the emergence of new palpable tumors during treatment, even eliminating microscopic hyperplasia. This suggests that early-stage tumors are more immunologically active and responsive to ICI therapies than more advanced-stage tumors, consistent with clinical observations in breast cancer patients (39). Histological and scRNA-seq analyses of normal mammary glands without palpable tumors from NMU-treated rats revealed a significant reduction in overall epithelial content, with a marked decrease in progenitor-like cells. Our findings suggest that short-term ICI treatment in high-risk women could potentially reduce breast cancer risk, although the immune-related side effects make this unlikely to be a feasible cancer preventive approach.

The A-196 KMT5B/C inhibitor demonstrated the highest efficacy when combined with αPD-L1 establishing this combination as a promising strategy to improve ICI efficacy in ER-positive breast cancer. H4K20me3 is a key epigenetic regulator of chromatin function, influencing various cellular processes including proliferation, DNA repair, genomic stability, immune responses, and cell cycle control (40). Our most significant finding was the emergence of multiple unique tumor epithelial cell subpopulations in the A-196 treatment group, accompanied by an increase in basal signatures in luminal progenitors, indicative of epigenetic reprogramming. These observations are consistent with similar findings in pancreatic (41), hepatocellular (26), and colorectal cancer (42), where KMT5C and H4K20me3 have been implicated in regulating EMT and stemness phenotypes. The observed changes in cell state were also associated with increased expression of genes involved in antigen presentation, providing a rationale for combining KMT5B/C inhibition with ICI therapy.

In summary, while the variability in tumor onset and growth rates in our rat NMU-induced mammary tumor model poses challenges with interpreting treatment results and necessitates large cohorts, our results align with clinical data and highlight the utility of this model for preclinical studies of ER-positive breast cancer. Additionally, while scRNA-seq provided granular insights into the cell type–specific effects of the treatments, functional validation of the roles of specific cell types and key pathways is essential to elucidate their contributions to tumor growth and therapeutic responses. Nonetheless, we have identified KMT5B/C as a modulator of response to ICI therapy, warranting further investigation of its therapeutic potential in ER-positive and other cancer types.

Materials and Methods

Animal Experiments. Animal experiments were conducted following protocol #15-055, approved by the DFCI Institutional Animal Care and Use Committee (IACUC), and adhered to NIH guidelines. All animals were housed at the Longwood Center Association for Assessment and Accreditation of Laboratory Animal Care International–approved facility at Dana-Farber Cancer Institute (DFCI, Boston, MA). Virgin Sprague-Dawley (SD:Hsd) female rats, aged 3 to 4 wk (weighing 45 to 50 g), were purchased from Envigo. Tumors were induced by intraperitoneal injection of 50 mg/kg NMU (MedChemExpress, HY-34758) on days 46 and 53 of age. Rats were randomly assigned to treatment groups, and tumor size was measured every other day using calipers. Treatment with NIS793 (Novartis, NVS-NBC/Koelln Lab, NIS793UFT, IPROT#APP-9714JF-94-GC04), TBK1/IKKε-IN-5 (Shanghai Medicilon, Inc., CAS1893397-65-3), A-196 (MedChemExpress, HY-100201), fulvestrant (MedChemExpress, HY-13636), αPD-L1, or a combination of targeted therapy with αPD-L1was initiated when tumors reached 8 mm in size, more than one tumor was detected, or a tumor remained unchanged in size for more than three days. NIS793 was diluted in PBS and stored at 4 °C for up to 6 mo. IKBKEi was prepared in hydroxypropyl methylcellulose K100LV, Tween 80, and 0.05 N hydrochloric acid, and stored at 4 °C for up to seven days. A-196 was dissolved in 10% DMSO and 90% corn oil and stored at 4 °C for up to 7 d. Fulvestrant was freshly prepared in a vehicle consisting of ethyl alcohol, benzyl alcohol, benzyl benzoate, and castor oil. Treatments were administered by oral gavage for IKBKEi (40 mg/kg) and A-196 (25 mg/kg), by intraperitoneal injection for αPD-L1 (10 mg/kg), and by intramuscular injection for fulvestrant (10 mg/kg), according to specific drug schedules for up to 6 wk. Anti-rat PD-L1 (clone 368.A.4H1, mouse IgG1, kappa) was produced in the Freeman lab by immunizing CD274 and PDCD1LG2-deficient mice with a human PD-L1-Fc fusion protein, following a previously reported protocol (43, 44). The product contained <2 endotoxin units/mg protein. Clone 368.A.4H1 [RRID:AB_2910261; (45)] has been shown to bind rat PD-L1 with high affinity and block its interaction with PD-1, and was therapeutically validated in prior studies (5). αPD-L1 or IgG1 isotype control (BioXcell, BE0083) was administered weekly at 10 mg/kg via intraperitoneal injection for six consecutive weeks. While each rat was intended to receive a full course of treatment (4 wk for monotherapies, 6 wk for combination therapies), treatment was administered only on weekdays. This was due to logistical constraints at the animal facility, including lack of weekend staff to assist with procedures such as oral gavage and concerns about managing potential treatment-related complications. In addition, based on observations from our pilot studies, and early signs of mild weight loss in some groups during this experiment, we introduced treatment-free weekends as intentional "treatment holidays" to reduce cumulative toxicity and support animal welfare. Tumors and mammary glands were harvested and processed for paraffin embedding or tissue digestion. A slice of the largest cross-section was preserved for histological analysis, fixed in 10% formalin overnight, stored in 70% ethanol, and paraffin-embedded for histological slide preparation. The remaining tumor tissue was dissociated into single-cell suspensions for flow cytometry or scRNA-seq library preparation. Tissue digestion was performed using 2 mg/mL collagenase type IV (Worthington, LS004189) in DMEM/F12 (Thermo Fisher Scientific, MT10090CV) with constant stirring at 37 °C for 1 to 2 h.

Tumor Growth Measurements and Classification of Growth Patterns. 37 small tumors in a total of 56 rats were discovered either a few days before tissue collection or during the collection process. Due to insufficient data to calculate a growth curve, these tumors were excluded from the tumor growth and cumulative growth rate calculations. Tumor growth rates were quantified as the "diametrical growth rate," calculated using linear regression of all recorded tumor diameter measurements over time, as described previously (5). To classify tumors as stable or growing, the second derivative of the growth curve was computed to represent the curve's slope. Tumors were then categorized based on the median value of all tumors: those with values below the median were classified as stable, while those above the median were classified as growing. Unclassified tumors are those with insufficient data points or ambiguous growth trends that did not allow for a confident classification. The cumulative growth rate (CGR) was determined using the following formula:

$$\mathrm{CGR} = \sum_{i=0}^{f=t(\mathit{euthanasia})} \frac{\text{Volume final}}{\text{Volume initial}}^{\left(\frac{1.303}{t}-1\right)} \times 100\,\%.$$

Single Cell RNA-seq Library Preparation. For single-cell RNA sequencing (scRNA-seq) of tumors and whole mammary glands, viable cells were resuspended in PBS containing 0.04% BSA at a concentration of 1,000 cells/μL. A total of 10,000 cells were loaded onto a 10× Genomics Chromium™ instrument (10× Genomics) following the manufacturer's protocol. scRNA-seq libraries were constructed using the Chromium Next GEM Single Cell 5′ HT v2 kit (10× Genomics). Quality control of the amplified cDNA and final sequencing libraries was conducted using the Bioanalyzer High Sensitivity DNA Kit (Agilent). The pooled libraries were sequenced on an Illumina NovaSeq S4 platform.

RNA-seq Library Preparation. Approximately 30 mg of snap-frozen tumor tissue was mechanically homogenized, and total RNA was isolated using silica-membrane column purification (RNeasy Mini Kit, QIAGEN) following the manufacturer's protocol, including on-column DNase treatment. RNA quantity and integrity were assessed by fluorometric assay and capillary electrophoresis. mRNA was enriched by poly(A) selection, according to the manufacturer's instructions. Libraries were quantified and normalized, pooled equimolarly, and sequenced on an Illumina NovaSeq platform to a target depth of ~30 million reads per sample.

Histology and Immunofluorescence Staining. Multicolor immunofluorescence, trichrome, and hematoxylin–eosin (H&E) analyses were performed as described previously (46). Briefly, after heat-induced antigen retrieval in sodium

citrate (pH = 6) or TRIS-EDTA buffer (pH = 9), the samples blocked with 10% goat serum (Thermo Fisher Scientific, 16210072) and stained with various antibodies at the indicated dilutions. *SI Appendix*, Table S1 includes information on antigen retrieval conditions, antibody identity, and antibody dilution. Stained slides were imaged using a Nikon Eclipse Ti2 microscope, or Olympus VS200 slide scanner at the Neurobiology Imaging Facility at Harvard and quantified using QuPath (47). For quantifications, tumor sections were prepared from all collected tumors. In cases of large tumors, multiple nonoverlapping sections were taken to account for potential heterogeneity within the tumor. Each section was treated as an independent measurement. To ensure consistency across groups, the same sampling approach was applied to all tumors. Comparisons between treatment groups were conducted using nonparametric statistical tests, with pairwise comparisons made against the vehicle control group. Statistical analyses accounted for the variability introduced by multiple sections from the same tumor.

Flow Cytometry. Tumor immune cell composition was analyzed using flow cytometry. Tumors were harvested and dissociated to single cells as described above. Lymphocytes and myeloid cells were evaluated using separate antibody panels. Single-cell suspensions were first stained with Live/Dead Aqua and an Fc-blocking antibody at 4 °C for 20 min. For the lymphocyte panel, cells were stained with surface markers in FACS buffer (0.5% BSA, 1% FBS, and 4 mM EDTA) on ice for 1 h, followed by intracellular marker staining after fixation and permeabilization. For the myeloid panel, cells were initially incubated with unconjugated primary antibodies and corresponding secondary antibodies, followed by staining with the remaining conjugated antibodies. Unstained cells served as negative controls, and single-stained and Fluorescence Minus One (FMO) controls were used for gating. Data acquisition was performed using a BD LSR Fortessa cell analyzer, and FlowJo software (Becton Dickinson, version 10.8.2) was used for data analysis and visualization. Gating strategies are provided in *SI Appendix*, Figs. S2 and S3, and antibodies used for flow cytometry are detailed in *SI Appendix*, Table S1.

Single Cell RNA-seq Analyses. Sequenced reads were processed and aligned to the rat reference genome (Rnor_6) using 10× Genomics Cell Ranger (version 6.1.2). The resulting data were imported into Seurat R package (version 4.4.0) (48) and subjected to stringent filtering criteria to exclude cells with a) nCount_RNA < 5,000, b) percent_mito > 20%, and c) percent_ribo < 40%. After filtering, 21,358 genes were detected across 120,095 cells, distributed by treatment as follows: Vehicle: 10,333 cells; αPD-L1: 8,109 cells; NIS793: 10,929 cells; αPD-L1 + NIS793: 8,325 cells; Fulvestrant: 15,205 cells; αPD-L1 + Fulvestrant: 15,205 cells; IKBKEi: 9,266 cells; αPD-L1 + IKBKEi: 9,461 cells; A-196: 19,068 cells; and αPD-L1 + A-196: 16,661 cells. The filtered data were normalized using *SCTransform*, and doublets were detected using scDblFinder R package (version 1.16.0) (49), cells classified as doublets were removed. Control mammary gland scRNA-seq samples were obtained from our prior study (7) (GEO accession: GSE184095), which included NMU-treated but tumor-free mammary glands, and processed using the same filtering and normalization criteria for integration and comparison. Additional mammary gland samples were derived from our own experiment, in which rats were treated with NMU but did not have macroscopic lesions. These glands were harvested from animals treated with fulvestrant or the αPD-L1 + fulvestrant combination, following the same tissue processing and sequencing protocols. A total of 64,836 cells were recovered from these samples: Vehicle: 29,277; Fulvestrant: 11,905 cells; αPD-L1 + Fulvestrant: 23,654 cells. All samples were integrated using the Harmony algorithm, with batch identity used as the integration variable to correct for technical differences.

To streamline the analysis, samples were subset by treatment group. Vehicle and αPD-L1 single treatments were used as controls, while each target treatment, both alone and in combination with αPD-L1 was included. The resulting subset was integrated using Harmony R package (version 1.2.0) (50). After we performed a dimensional reduction with principal component analysis (PCA). Neighborhood graphs were computed using the *FindNeighbors*() function, with dimensional inputs ranging from 10 to 75. Clustering was performed with the *FindClusters*() function at a resolution of 0.1 to 0.5. Uniform Manifold Approximation and Projection (UMAP) embeddings were computed using the first 75 PCA dimensions, with specific inputs adjusted based on the treatment group or subcluster analyzed.

To properly subseT cell types within our dataset, we applied a keratin gene filter (*SI Appendix*, Table S2). All keratin genes present in the expression matrix were extracted, and cells expressing at least two or more keratin genes were classified as epithelial cancer cells. For immune cells, we applied a filter using 28 immune-related genes (*SI Appendix*, Table S2). Cells with more than one read for these genes in the RNA expression matrix were classified as immune cells. Cells that were double-negative for both keratin and immune gene filters were further subset. Using differential expression analysis from the *FindAllMarkers*() function, these cells were assigned to stromal clusters, such as fibroblasts, endothelial cells, and pericytes. The double positive cells were excluded, as they exhibited a pattern suggestive of contamination, with coexpression of keratin and immune cell marker genes that are unlikely to coexist within the same cell. Cell subtypes were identified by analyzing the expression of well-established markers and the top differentially expressed genes (DEGs) defining each cluster. Differential expression analysis was performed using the *FindMarkers*() function in Seurat, employing the default Wilcoxon rank-sum test. DEG lists were refined by applying a corrected p-value threshold (p_val_adj ≤ 0.05) and an absolute log2(fold change) ≥ 0.25. For an in-depth analysis of various cancer hallmarks from gene set enrichment analysis (GSEA) (51, 52), gene modules were applied using the *AddModuleScore*() function to calculate scores across clusters or treatment groups. GSEA of the DEGs identified through *FindAllClusters*() was conducted using GSEA software, focusing on pathways with significant p-values and highlighting the number of genes contributing to the enrichment of each pathway.

Differential abundances (DA) between growing and stable cells in the fulvestrant treatment setup were calculated using Milo neighborhood analysis R package (version 1.10.0) (15). A Milo KNN graph was constructed by scaling cells with unique identifiers based on sequencing depth, log-transforming their expression matrices, and projecting them onto major principal components. The *buildGraph*() function was used with parameters k = 30 and d = 30 to define the KNN graph. Cell neighborhoods and their connectivity were then determined by summing neighborhood indices and their connections along individual KNN graph edges. *P*-values were adjusted using a weighted Benjamini–Hochberg method, accounting for the reciprocal of neighborhood connectivity. In the KNN graph, each node represents a neighborhood, with the node size corresponding to the number of cells within the neighborhood. Edges represent the overlap of cells between neighborhoods. Node coordinates were derived from the indexed single cells projected onto the UMAP cell embedding. The distribution of DA fold changes for each neighborhood, significantly skewed toward specific growing or stable condition, and was visualized using a beeswarm plot via *plotDAbeeswarm*(). To identify neighborhood DA expression markers, the *FindNhoodGroupMarkers*() function was employed, enabling the derivation of neighborhood identities. Cell–cell communication analysis was performed using the CellChat R package (version 1.6.1) (23, 24) to infer, analyze, and visualize intercellular signaling in the mammary gland dataset. Raw expression data and metadata were imported into a CellChat object, with cell groups defined according to annotated clusters. To specifically investigate signaling between AL Kit^{+} and ML-HR^{high} epithelial populations and T cells, we subsetted these clusters and merged them with the immune compartment. Network-level interactions were visualized using circular net plots, *netVisual_circle*(), to assess interaction strength and directionality between sender and receiver cell types. Communication probability dot plots, *netVisual_bubble*(), were used to display the top ligand–receptor pairs mediating the interaction between epithelial clusters and T cell subsets.

RNA-seq Analyses. RNA-seq data were analyzed using the VIPER pipeline (53). Briefly, reads were aligned to the Rattus norvegicus reference genome (Rnor_6) using STAR (54). Genes with zero counts across all samples were excluded, and the remaining counts were normalized using the log2-transformed trimmed mean of M values (log2*TMM–CPM*+ 1TMM–CPM + 1) as implemented in edgeR (version 4.0.15) (55) for exploratory analyses and visualization. For differential expression analysis, raw (nonnormalized) counts were analyzed with DESeq2 R package (version 1.42.0) (56), specifying treatment groups as factor levels.

Public Dataset Analyses. Fulvestrant-resistance signature enrichment analysis was performed using RNA-seq data from a published study (19). Signature enrichment scores were calculated using the GSVA package (57) and compared between resistant and responsive biopsies paired by patient. Androgen receptor (AR) expression and hallmark AR signaling signature enrichment analyses were conducted using the same method and applied to RNA-seq or microarray datasets from three independent clinical cohorts: the POETIC trial (58), the Z1031B cohort (59), and the Guerrero-Zotano et al. dataset (16).

Statistical Analyses. If the data for matched comparisons did not meet the normal distribution criteria, nonparametric tests were employed. In the case of single comparisons with normal distribution, Student's *t* test was performed. For the nonpaired single comparisons, Mann–Whitney or Wilcoxon tests were utilized. For multiple comparisons, a one-way ANOVA corrected for multiple comparisons was applied or in case of nonparametric distributions Kruskal–Wallis was used. All statistical analyses were conducted with a 95% CI, and corresponding significant *P*-values ($P > 0.05$) were provided for each experiment. To identify significant differences between single-cell populations, variability in total cell populations and across clusters was accounted for using a permutation test. A *P*-value for each cluster was calculated based on 1,000 permutations, and the magnitude of the differences was quantified by bootstrapping to generate a CI for the log2 fold change (log2FC). Populations were considered significant if they met the criteria of FDR < 0.05 and absolute log2FC > 0.58. Significant populations that had an increase compared to the vehicle are shown.

Data, Materials, and Software Availability. scRNA-seq data have been deposited in NCBI GEO (GSE284698) (60). Other data are included in the article and/or supporting information.

ACKNOWLEDGMENTS. We thank members of our laboratory for their critical reading of this manuscript and insightful discussions. This research was supported by the Novartis Institute for Biomedical Research (K.P.), National Cancer Institute T32 CA236754 (T.M.B.), NIH P01 AI056299 (G.J.F.), Charles King Foundation (Z.L.), Belgian American Educational Foundation (P.F.), and the Breast Cancer Research Foundation (K.P.). K.P. receives sponsored research funding through Dana-Farber from Novartis that in part funded this study.

1. H. J. Burstein *et al.*, Endocrine treatment and targeted therapy for hormone receptor-positive, human epidermal growth factor receptor 2-negative metastatic breast cancer: ASCO guideline update. *J. Clin. Oncol.* **39**, 3959–3977 (2021).
2. S. H. Giordano *et al.*, Systemic therapy for advanced human epidermal growth factor receptor 2-positive breast cancer: ASCO guideline update. *J. Clin. Oncol.* **40**, 2612–2635 (2022).
3. G. Di Grazia *et al.*, Unlocking the potential of immune checkpoint inhibitors in HR+/HER2- breast cancer: A systematic review. *Cancers (Basel)* **17**, 2940 (2025).
4. R. Nicotra, C. Lutz, H. A. Messal, J. Jonkers, Rat models of hormone receptor-positive breast cancer. *J. Mammary Gland Biol. Neoplasia* **29**, 12 (2024).
5. C. R. Gil Del Alcazar *et al.*, Insights into immune escape during tumor evolution and response to immunotherapy using a rat model of breast cancer. *Cancer Immunol. Res.* **10**, 680–697 (2022).
6. P. Yan *et al.*, Midkine as a driver of age-related changes and increase in mammary tumorigenesis. *Cancer Cell* **42**, 1936–1954.e9 (2024).
7. M. Alečković *et al.*, Breast cancer prevention by short-term inhibition of TGFβ signaling. *Nat. Commun.* **13**, 7558 (2022).
8. J. S. Boehm *et al.*, Integrative genomic approaches identify IKBKE as a breast cancer oncogene. *Cell* **129**, 1065–1079 (2007).
9. R. W. Jenkins *et al.*, Ex vivo profiling of PD-1 blockade using organotypic tumor spheroids. *Cancer Discov.* **8**, 196–215 (2018).
10. K. D. Bromberg *et al.*, The SUV4-20 inhibitor A-196 verifies a role for epigenetics in genomic integrity. *Nat. Chem. Biol.* **13**, 317–324 (2017).
11. D. Bedinger *et al.*, Development and characterization of human monoclonal antibodies that neutralize multiple TGFbeta isoforms. *MAbs* **8**, 389–404 (2016).
12. H. Lind *et al.*, Dual targeting of TGF-beta and PD-L1 via a bifunctional anti-PD-L1/TGF-betaRII agent: Status of preclinical and clinical advances. *J. Immunother. Cancer* **8**, e000433 (2020).
13. M. Shipitsin *et al.*, Molecular definition of breast tumor heterogeneity. *Cancer Cell* **11**, 259–273 (2007).
14. W. Chen *et al.*, Chronic type I interferon signaling promotes lipid-peroxidation-driven terminal CD8(+) T cell exhaustion and curtails anti-PD-1 efficacy. *Cell Rep.* **41**, 111647 (2022).
15. E. Dann, N. C. Henderson, S. A. Teichmann, M. D. Morgan, J. C. Marioni, Differential abundance testing on single-cell data using k-nearest neighbor graphs. *Nat. Biotechnol.* **40**, 245–253 (2022).
16. A. L. Guerrero-Zotano *et al.*, ER(+) breast cancers resistant to prolonged neoadjuvant letrozole exhibit an E2F4 transcriptional program sensitive to CDK4/6 inhibitors. *Clin. Cancer Res.* **24**, 2517–2529 (2018).
17. I. Bozovic-Spasojevic *et al.*, The prognostic role of androgen receptor in patients with early-stage breast cancer: A meta-analysis of clinical and gene expression data. *Clin. Cancer Res.* **23**, 2702–2712 (2017).
18. S. Massarweh *et al.*, A phase II neoadjuvant trial of anastrozole, fulvestrant, and gefitinib in patients with newly diagnosed estrogen receptor positive breast cancer. *Breast Cancer Res. Treat.* **129**, 819–827 (2011).
19. Y. Xia *et al.*, Integrated DNA and RNA sequencing reveals drivers of endocrine resistance in estrogen receptor-positive breast cancer. *Clin. Cancer Res.* **28**, 3618–3629 (2022).
20. J. Albrecht *et al.*, Dynamic methylation and expression of alternative promoters for oestrogen receptor alpha in cell line models of fulvestrant resistance. *Mol. Oncol.* **19**, 204–224 (2024), 10.1002/1878-0261.13713.
21. J. Finlay-Schultz *et al.*, Breast cancer suppression by progesterone receptors is mediated by their modulation of estrogen receptors and RNA polymerase III. *Cancer Res.* **77**, 4934–4946 (2017).
22. C. W. Yde, K. B. Emdal, B. Guerra, A. E. Lykkesfeldt, NFκB signaling is important for growth of antiestrogen resistant breast cancer cells. *Breast Cancer Res. Treat.* **135**, 67–78 (2012).
23. S. Jin, M. V. Plikus, Q. Nie, Cell chat for systematic analysis of cell-cell communication from single-cell transcriptomics. *Nat. Protoc.* **20**, 180–219 (2025).
24. S. Jin *et al.*, Inference and analysis of cell-cell communication using Cell Chat. *Nat. Commun.* **12**, 1088 (2021).
25. A. Mary, R. Mancuso, M. T. Heneka, Immune activation in Alzheimer disease. *Annu. Rev. Immunol.* **42**, 585–613 (2024).
26. L. Yu *et al.*, H4-methylation regulators mediated epitranscriptome patterns and tumor microenvironment infiltration characterization in hepatocellular carcinoma. *Clin. Epigenet.* **15**, 43 (2023).
27. Y. Sun *et al.*, Targeting TBK1 to overcome resistance to cancer immunotherapy. *Nature* **615**, 158–167 (2023).
28. A. Ribas, J. D. Wolchok, Cancer immunotherapy using checkpoint blockade. *Science* **359**, 1350–1355 (2018).
29. T. E. Keenan, S. M. Tolaney, Role of immunotherapy in triple-negative breast cancer. *J. Natl. Compr. Canc. Netw.* **18**, 479–489 (2020).
30. H. S. Rugo *et al.*, Safety and antitumor activity of pembrolizumab in patients with estrogen receptor–positive/human epidermal growth factor receptor 2–negative advanced breast cancer. *Clin. Cancer Res.* **24**, 2804–2811 (2018).
31. N. K. Andresen *et al.*, Ipilimumab and nivolumab combined with anthracycline-based chemotherapy in metastatic hormone receptor-positive breast cancer: A randomized phase 2b trial. *J. Immunother. Cancer* **12**, e007990 (2024).
32. A. Rios-Hoyo *et al.*, Neoadjuvant chemotherapy and immunotherapy for estrogen receptor-positive human epidermal growth factor 2-negative breast cancer. *J. Clin. Oncol.* **42**, 2632–2636 (2024).
33. J. L. Gulley *et al.*, Dual inhibition of TGF-beta and PD-L1: A novel approach to cancer treatment. *Mol. Oncol.* **16**, 2117–2134 (2022).
34. C. H. Stuelten, Y. E. Zhang, Transforming growth factor-beta: An agent of change in the tumor microenvironment. *Front. Cell Dev. Biol.* **9**, 764727 (2021).
35. T. M. Bauer *et al.*, Phase I/Ib, open-label, multicenter, dose-escalation study of the anti-TGF-β monoclonal antibody, NIS793, in combination with spartalizumab in adult patients with advanced tumors. *J. Immunother. Cancer* **11**, e007353 (2023).
36. R. Jeselsohn *et al.*, TransCONFIRM: Identification of a genetic signature of response to fulvestrant in advanced hormone receptor-positive breast cancer. *Clin. Cancer Res.* **22**, 5755–5764 (2016).
37. M. Gil-Gil *et al.*, Prognostic value of PAM50 in residual breast cancer following neoadjuvant endocrine therapy (NET): A retrospective analysis with long follow-up. *J. Clin. Oncol.* **37**, 15_suppl.575 (2019).
38. C. Ricciardelli *et al.*, The magnitude of androgen receptor positivity in breast cancer is critical for reliable prediction of disease outcome. *Clin. Cancer Res.* **24**, 2328–2341 (2018).
39. M. A. Harris *et al.*, Towards targeting the breast cancer immune microenvironment. *Nat. Rev. Cancer* **24**, 554–577 (2024).
40. A. Agredo, A. L. Kasinski, Histone 4 lysine 20 tri-methylation: A key epigenetic regulator in chromatin structure and disease. *Front. Genet.* **14**, 1243395 (2023).
41. M. Viotti *et al.*, SUV420H2 is an epigenetic regulator of epithelial/mesenchymal states in pancreatic cancer. *J. Cell Biol.* **217**, 763–777 (2018).
42. V. Boonsanay *et al.*, Loss of SUV420H2-dependent chromatin compaction drives right-sided colon cancer progression. *Gastroenterology* **164**, 214–227 (2023).
43. D. A. Reardon *et al.*, Glioblastoma eradication following immune checkpoint blockade in an orthotopic immunocompetent model. *Cancer Immunol. Res.* **4**, 124–135 (2016).
44. J. A. Brown *et al.*, Blockade of programmed death-1 ligands on dendritic cells enhances T cell activation and cytokine production. *J. Immunol.* **170**, 1257–1266 (2003).
45. A. Chaudhri *et al.*, PD-L1 binds to B7-1 only in cis on the same cell surface. *Cancer Immunol. Res.* **6**, 921–929 (2018).
46. C. R. Gil Del Alcazar *et al.*, Immune escape in breast cancer during in situ to invasive carcinoma transition. *Cancer Discov.* **7**, 1098–1115 (2017).
47. P. Bankhead *et al.*, QuPath: Open source software for digital pathology image analysis. *Sci. Rep.* **7**, 16878 (2017).
48. Y. Hao *et al.*, Integrated analysis of multimodal single-cell data. *Cell* **184**, 3573–3587.e29 (2021).
49. P. L. Germain, A. Lun, C. Garcia Meixide, W. Macnair, M. D. Robinson, Doublet identification in single-cell sequencing data using scDblFinder. *F1000Res* **10**, 979 (2021).
50. I. Korsunsky *et al.*, Fast, sensitive and accurate integration of single-cell data with harmony. *Nat. Methods* **16**, 1289–1296 (2019).
51. A. Subramanian *et al.*, Gene set enrichment analysis: A knowledge-based approach for interpreting genome-wide expression profiles. *Proc. Natl. Acad. Sci. U.S.A.* **102**, 15545–15550 (2005).
52. V. K. Mootha *et al.*, PGC-1alpha-responsive genes involved in oxidative phosphorylation are coordinately downregulated in human diabetes. *Nat. Genet.* **34**, 267–273 (2003).
53. M. Cornwell *et al.*, VIPER: Visualization pipeline for RNA-seq, a Snakemake workflow for efficient and complete RNA-seq analysis. *BMC Bioinformatics* **19**, 135 (2018).
54. A. Dobin *et al.*, STAR: Ultrafast universal RNA-seq aligner. *Bioinformatics* **29**, 15–21 (2013).
55. M. D. Robinson, D. J. McCarthy, G. K. Smyth, edgeR: A Bioconductor package for differential expression analysis of digital gene expression data. *Bioinformatics* **26**, 139–140 (2010).
56. M. I. Love, W. Huber, S. Anders, Moderated estimation of fold change and dispersion for RNA-seq data with DESeq2. *Genome Biol.* **15**, 550 (2014).
57. S. Hanzelmann, R. Castelo, J. Guinney, GSVA: Gene set variation analysis for microarray and RNA-seq data. *BMC Bioinformatics* **14**, 7 (2013).
58. E. F. Schuster *et al.*, Molecular profiling of aromatase inhibitor sensitive and resistant ER+HER2- postmenopausal breast cancers. *Nat. Commun.* **14**, 4017 (2023).
59. M. J. Ellis *et al.*, Ki67 proliferation index as a tool for chemotherapy decisions during and after neoadjuvant aromatase inhibitor treatment of breast cancer: Results from the American College of Surgeons Oncology Group Z1031 trial (Alliance). *J. Clin. Oncol.* **35**, 1061–1069 (2017).
60. E. Rojas*et al.*, Single-cell RNA sequencing of rat mammary tumors treated with epigenetic and endocrine therapies. NCBI Gene Expression Omnibus. https://www.ncbi.nlm.nih.gov/geo/query/acc.cgi?acc=GSE284698. Deposited 8 August 2025.